LETTER

Mitochondrial uncoupling protein 2 structure determined by NMR molecular fragment searching

Marcelo J. Berardi[1,2], William M. Shih[2,3,4], Stephen C. Harrison[1,2,5] & James J. Chou[1,2]

Mitochondrial uncoupling protein 2 (UCP2) is an integral membrane protein in the mitochondrial anion carrier protein family, the members of which facilitate the transport of small molecules across the mitochondrial inner membrane[1,2]. When the mitochondrial respiratory complex pumps protons from the mitochondrial matrix to the intermembrane space, it builds up an electrochemical potential[2]. A fraction of this electrochemical potential is dissipated as heat, in a process involving leakage of protons back to the matrix[2]. This leakage, or 'uncoupling' of the proton electrochemical potential, is mediated primarily by uncoupling proteins[2]. However, the mechanism of UCP-mediated proton translocation across the lipid bilayer is unknown. Here we describe a solution-NMR method for structural characterization of UCP2. The method, which overcomes some of the challenges associated with membrane-protein structure determination[3], combines orientation restraints derived from NMR residual dipolar couplings (RDCs) and semiquantitative distance restraints from paramagnetic relaxation enhancement (PRE) measurements. The local and secondary structures of the protein were determined by piecing together molecular fragments from the Protein Data Bank that best fit experimental RDCs from samples weakly aligned in a DNA nanotube liquid crystal. The RDCs also determine the relative orientation of the secondary structural segments, and the PRE restraints provide their spatial arrangement in the tertiary fold. UCP2 closely resembles the bovine ADP/ATP carrier (the only carrier protein of known structure[4]), but the relative orientations of the helical segments are different, resulting in a wider opening on the matrix side of the inner membrane. Moreover, the nitroxide-labelled GDP binds inside the channel and seems to be closer to transmembrane helices 1–4. We believe that this biophysical approach can be applied to other membrane proteins and, in particular, to other mitochondrial carriers, not only for structure determination but also to characterize various conformational states of these proteins linked to substrate transport.

The elucidation almost 50 years ago of the mechanism of oxidative phosphorylation provided the first example of the coupling of membrane transport to energy production[5]. The mitochondrial respiratory complex transfers electrons from nutrients to oxygen, pumping protons from the mitochondrial matrix to the intermembrane space as it builds up an electrochemical potential of ~200 mV (Supplementary Fig. 1). Most of this potential is converted to work that drives ATP synthesis, but a fraction is dissipated as heat in the uncoupling of the proton electrochemical potential by members of a family of proteins in the mitochondrial inner membrane, collectively termed uncoupling proteins[2] (UCPs). The proton translocation activity of UCPs requires fatty acids as cofactors; it is inhibited by GDP. UCP1 was first identified in the mitochondria of brown adipose tissue as a protein responsible for thermoregulation mediated by such tissue[6]. Unlike UCP1, the primary function of UCP2 may be related to lowering production of reactive oxygen species[2]. Expression of UCP2 in pancreatic β-cells is strongly correlated with decreased insulin secretion, and UCP2 inactivation restores the glucose-sensing pathway[7]. UCP2 also has a role in glucagon secretion from pancreatic α-cells[8] and in regulation of hunger by means of ghrelin in neurons containing neuropeptide Y and agouti-related protein[9]. More recently, UCP2 has been linked to chemotherapy resistance and metabolic reprogramming in cancer[10,11].

NMR spectroscopy has yielded the structures of a number of membrane proteins, including channels[12–14], a redox protein[15], a kinase[16] and sensory rhodopsin[17]. In many of these studies, a major issue was the purification of the protein and its reconstitution in a model membrane medium supporting protein solubility and stability. In the case of UCP2, reconstitution in dodecylphosphocholine (DPC) micelles with a small amount of lipid (cardiolipin and dimyristoyl phosphatidylcholine (DMPC)) yielded usable NMR spectra (Fig. 1a, b). We prepared homogeneous UCP2 by passing detergent-solubilized protein through a GDP-analogue column, which selects for native protein. Samples used for NMR measurements were at pH 6.5 and contained 5 mM GDP, 150 mM DPC, 1 mM cardiolipin and 2 mM DMPC. Under those conditions, a fluorescence resonance energy transfer (FRET) experiment showed that GDP binds to UCP2 with an apparent dissociation constant of ~5 μM (Fig. 1c). When the NMR sample was incorporated into liposomes, it showed fatty-acid-activated and GDP-inhibited proton translocation activity (Supplementary Fig. 2). Negative-stain electron microscopy showed monodisperse, channel-like particles (Supplementary Fig. 3).

Local structure determination by NMR typically involves assigning nuclear Overhauser enhancements between backbone amide protons and aliphatic protons. In the case of UCP2, it was difficult to collect a sufficient number of unambiguous nuclear Overhauser enhancements because of severe overlap of backbone (^{1}H, ^{15}N) resonances. The peaks in the 3D HNCO spectrum are mostly separated, however. The HNCO experiment, which correlates the chemical shifts of backbone ^{1}H^N, ^{15}N and ^{13}C′ nuclides, has been widely used for measuring one-bond RDCs. For structure determination, we therefore relied on orientation restraints derived from RDCs. In a macromolecule marginally oriented in a magnetic field, the RDC between a pair of spin-1/2 nuclides encodes orientations of the internuclear vector connecting the two nuclides. The most effective medium for weakly orienting protein in solution is a liquid crystal formed by large, elongated particles[18]; for membrane proteins, these particles must also resist a high concentration of detergent. We used DNA nanotubes, constructed by 'DNA origami', which can form a stable nematic phase unaffected by detergent[19] (Supplementary Fig. 4). The nanotube alignment medium allowed us to measure RDCs for internuclear vectors ^{1}H^N–^{15}N ($^1D_{NH}$), ^{13}C′–^{13}C$^\alpha$ ($^1D_{C'C\alpha}$) and ^{15}N–^{13}C′ ($^1D_{NC'}$) (Fig. 1d and Supplementary Fig. 5). On average, there were 2.2 RDCs per residue for regions with confirmed resonance assignment.

With fewer than three RDCs per residue, calculating the local structures using the restrained molecular dynamics protocol presents a severe local minimum problem, because of the intrinsic orientation degeneracy of the dipolar coupling function. We used an approach that

[1]Jack and Eileen Connors Structural Biology Laboratory, Harvard Medical School, Boston, Massachusetts 02115, USA. [2]Department of Biological Chemistry and Molecular Pharmacology, Harvard Medical School, Boston, Massachusetts 02115, USA. [3]Department of Cancer Biology, Dana-Farber Cancer Institute, Boston, Massachusetts 02115, USA. [4]Wyss Institute for Biologically Inspired Engineering, Harvard University, Boston, Massachusetts 02138, USA. [5]Howard Hughes Medical Institute, Harvard Medical School, Boston, Massachusetts 02115, USA.
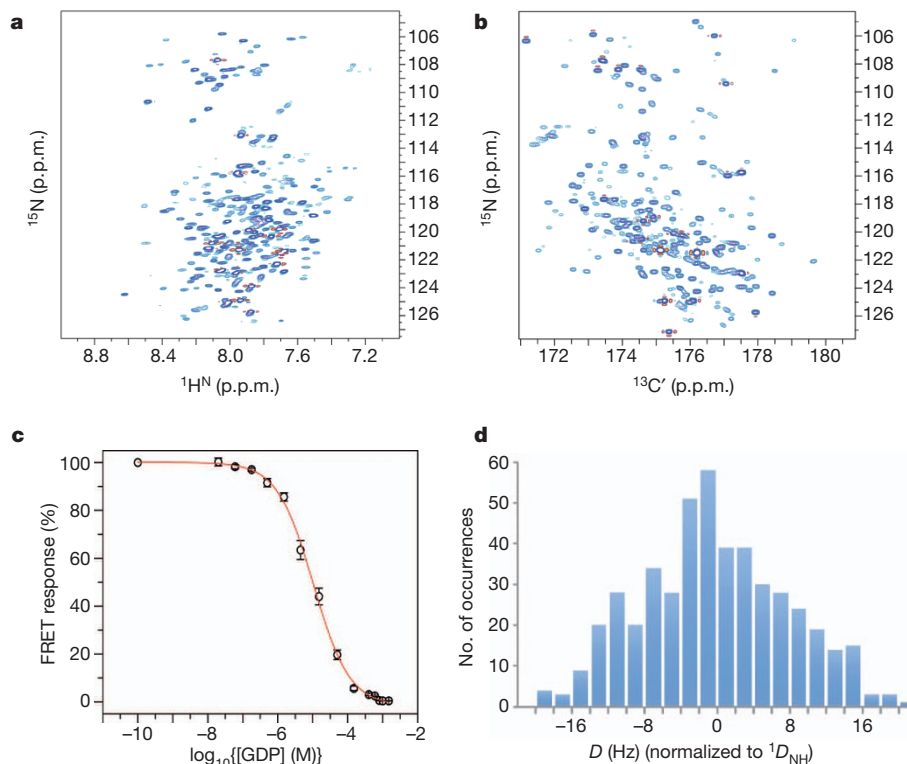
Figure 1 | NMR spectra, GDP binding and outline of RDC-based molecular fragment assignment. a, The $^1H^N$–^{15}N transverse-relaxation-optimized spectroscopy (TROSY) heteronuclear single quantum coherence spectrum of ^{15}N-, ^{13}C- and ^2H-labelled UCP2 reconstituted in DPC micelles (with 5 mM GDP), recorded at pH 6.5, 33 °C and a ^1H frequency of 600 MHz. **b**, The (^{15}N, $^{13}C'$) projection of the three-dimensional (3D) TROSY-HNCO spectrum of the sample in **a**, recorded under the same conditions. p.p.m., parts per million.

Comparison of **a** and **b** illustrates that most resonances can be resolved in the 3D HNCO spectrum. **c**, Specific binding of GDP to UCP2 under the conditions in **a**. The FRET response (Methods) follows displacement of fluorescent MANT-GDP by GDP as the concentration of the latter increases. [GDP], GDP concentration. **d**, Histogram of 470 unambiguously assigned vectors $^1D_{NH}$, $^1D_{C'C\alpha}$ or $^1D_{NC'}$ (all normalized to $^1D_{NH}$). The magnitude and rhombicity of the alignment tensors are 10 Hz and 0.61, respectively.

exhaustively searches the Protein Data Bank for fragments of structure that agree with the experimental data. This method, commonly known as molecular fragment replacement (MFR), was first applied in crystallography to build molecular fragments into crystallographically determined electron density[20]. A later NMR study demonstrated that with about four RDCs per residue, it was possible to determine the backbone structure of ubiquitin using molecular fragments fit to RDCs[21]. More recently, a fragment search method that combines experimentally determined chemical shift and RDCs has been implemented in the CS-ROSETTA structure modelling software and shown to be effective in determining structures of water-soluble proteins[22,23].

We constructed a database containing 320,000 seven-residue fragments extracted from structures of 1,279 water-soluble and 235 membrane-associated proteins. For each seven-residue stretch along the UCP2 sequence, we fitted the corresponding RDCs to all fragments in the database, using singular value decomposition[24]. We evaluated the quality of fit with the parameter Q_{free}, which is a normalized root mean squared difference between experimental RDCs and RDCs predicted independently by the structural model[25]. After this exhaustive search, we collected fragments with $Q_{free} < 25\%$ and for which the magnitude and rhombicity of the alignment tensor were within 10% of their true values (Fig. 1d). These 'candidate fragments' were used to determine local backbone structure according to a three-step protocol. The first step is 'fragment assignment', whereby the candidate fragments are sorted and those with the smallest Q_{free} values are assigned to the corresponding protein segments until no more fragments can be placed without overlap with already assigned segments (Fig. 2a). The second step is 'gap filling'. Here, for any of the gap regions (with fewer than four residues) not assigned in step one, we search for the candidate fragment that overlaps in the backbone dihedral angles ϕ and ψ with the two flanking fragments and that provides the lowest Q_{free}

value for the merged segment consisting of the newly filled gap structure and the two original flanking fragments (Fig. 2b). In the third step, 'end extension', we extend the amino- or carboxy-terminal end of an assigned segment by searching for a fragment that overlaps best with the original segment in ϕ and ψ, and that provides the lowest Q_{free} value for the final extended segment (Fig. 2b). Steps two and three were repeated until no more structure could be assigned with confidence. Using this procedure, we identified 15 structured segments (Fig. 2c).

In addition to RDCs, we obtained semiquantitative distance restraints from PRE measurements. The paramagnetic moiety introduced for PRE measurement is the nitroxide spin label in MTSL (Methods), which we covalently attached at cysteines. PRE restraints have been demonstrated in low-resolution structure determination of both water-soluble and membrane proteins[16,26]. Four UCP2 samples were produced, each with a spin label attached at a unique position (Cys 68, Cys 105, Cys 202 and Cys 255); they all showed similar NMR spectra (Supplementary Fig. 6). These samples together provided 452 PRE distance restraints (an important subset is shown in Fig. 3a).

Finally, to determine the tertiary structure, we strongly enforced the backbone ϕ and ψ of the 15 MFR-derived structural segments while applying the PRE and RDC restraints. During the structure calculation, the MFR segments made up most of the local structure of the protein, and the PRE and RDC measurements provided spatial and orientational restraints, respectively, for these structured segments. The calculation generated an ensemble of 15 structures with a backbone root mean squared deviation of 1.3 Å (Fig. 3b). There are no experimental data on the side chains. The structure was determined in the presence of GDP, a well-known inhibitor of UCP2 activity. Although side-chain resonance assignments, which are required to obtain an atomic-resolution view of GDP binding, were not available, we investigated GDP binding qualitatively by the PRE method. We
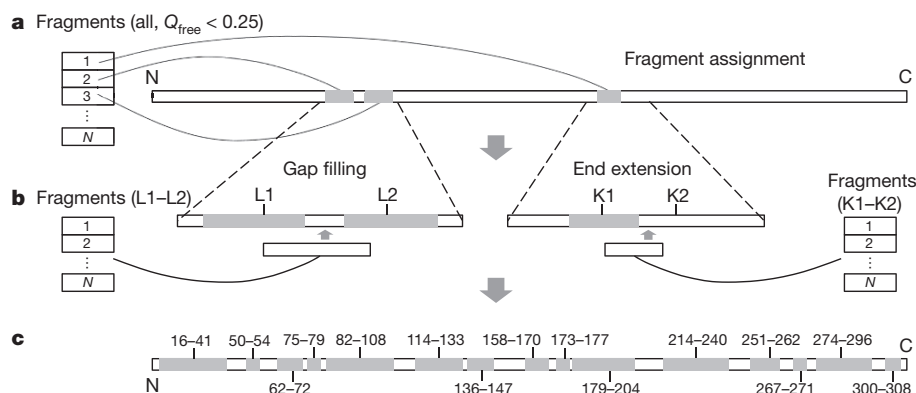
Figure 2 | Operations involved in RDC-based structural segment building. a, Initial fragment assignment. **b,** Gap filling (left) and end extension (right). **c,** The 15 continuous structured segments of UCP2 determined by RDC-based MFR (shaded and labelled). Details of these operations are described in the main text and in Methods.

used a paramagnetic nitroxide derivative of GDP (NO-GDP; Fig. 3c) and measured broadening of protein resonances by the spin label. Mapping the magnitude of the PRE to the structure indicates that NO-GDP binds within the UCP2 channel, but the PRE seems to span a large area, covering residues of transmembrane helices (TMHs) 1–4 (Fig. 3d). The distribution of PRE-sensitive residues indicates that the nitroxide radical is in the half of the channel facing the intermembrane space. On the basis of the PRE-derived position of the nitroxide moiety, we located the GDP portion of NO-GDP by maximizing electrostatic interactions between the GDP and charged residues in the channel (Supplementary Fig. 7). The model shows that the PRE data are consistent with GDP binding deep within the UCP2 channel, similar to the proposed ADP-binding site in ANT1[27,28] (also known as SLC25A4).

The overall conformation of UCP2 closely resembles that of the bovine ADP/ATP carrier[4] (ANT1), despite their low (~20%) sequence identity. They are both channel-like structures, in which three pseudo-repeats (Fig. 3a) adopt similar folds (Fig. 4a). Each repeat consists of a TMH (odd numbered), a loop, an amphipathic helix (APH) and a second TMH (even numbered). Moreover, as in ANT1, the TMHs have kinks at prolines that are conserved in the carrier-protein sequences (Fig. 3a). The structural similarity with ANT1 further supports the notion that the members of the large carrier family have a conserved structure and that small variations within the conserved fold govern the specificity of substrate binding and translocation. The most striking differences between the UCP2 and ANT1 structures are in the third repeat. In each of the three repeats of ANT1, the APH packs
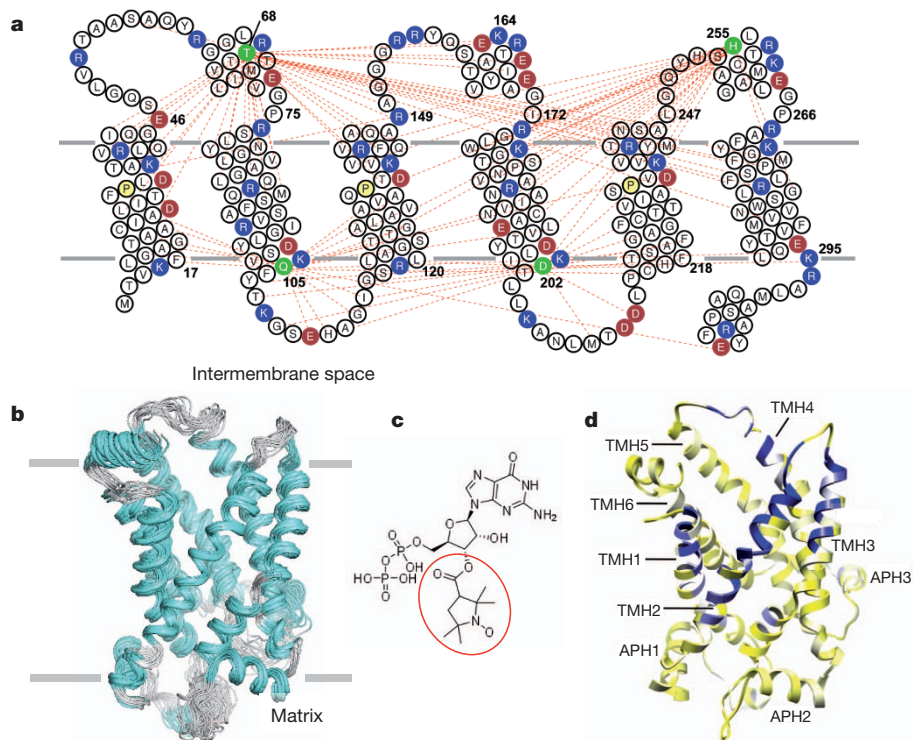
Figure 3 | Solution structure of UCP2 and region of GDP binding. a, UCP2 sequence and membrane topology, with basic and acidic residues shown in blue and red, respectively. The conserved prolines at the proline kinks of TMHs 1, 3 and 5 are shown in yellow. The spin-labelled positions are highlighted in green. The red dashed lines represent long-range or interhelical PRE distances (<19 Å) between the spin-label and backbone amide protons. **b,** An ensemble of 15 low-energy structures derived from NMR restraints. The backbone and heavy-atom root mean squared deviations for the structured segments in Fig. 2 are 1.2 and 1.8 Å, respectively. **c,** Chemical structure of the spin-labelled GDP, with the paramagnetic nitroxide moiety circled in red. **d,** Mapping the effect of spin-labelled GDP onto the ribbon drawing of UCP2. The colour gradient is from yellow (resonance intensity ratio of broadened to non-broadened, $\varepsilon = 1.0$) to white ($\varepsilon = 0.8$) to blue ($\varepsilon = 0.3$).
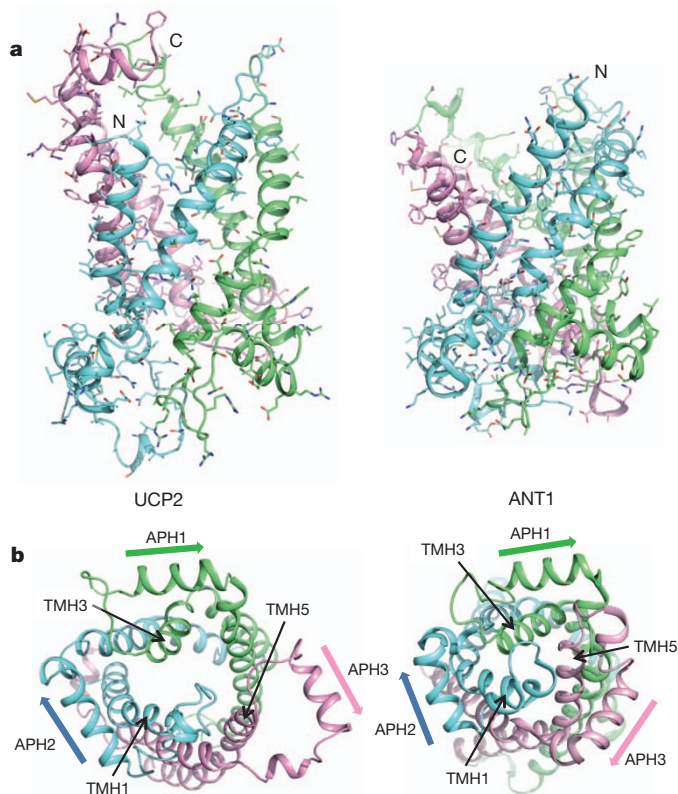
Figure 4 | Comparison of UCP2 and ANT1. a, Side views of UCP2 and ANT1 (Protein Data Bank ID, 1OKC). Pseudo-repeats one (residues 14–112), two (113–210) and three (211–309) are shown in blue, green and pink, respectively (see Fig. 3a for reference). **b,** Views of UCP2 and ANT1 from the matrix side of the carriers, showing loss of threefold pseudo-symmetry in UCP2 as a result of structural differences in repeat three. The orientations of the amphipathic helices are indicated by the arrows.

against the segment of the odd-numbered TMH that follows the conserved proline, and the proline kink in the TMH closes the channel (Fig. 4b). Repeat three of the GDP-bound UCP2 does not follow this pattern: TMH5 seems to have shifted between TMH4 and TMH6 towards the intermembrane side of the carrier (Supplementary Fig. 8). The APH of the same repeat rotates away from the channel by ~45°, and its flanking regions are also substantially different from their counterparts in the other two repeats (Fig. 4b). Consequently, the matrix side of the channel is substantially more open in UCP2 than in ANT1. Although their functional relevance remains to be investigated, the differences we see could have implications for channel opening in proteins of the carrier family.

More than 40 different mitochondrial carriers have so far been identified; they transport a variety of metabolites, nucleotides, ions and vitamins across the inner mitochondrial membrane. Although their overall folds are expected to be similar, obtaining structures of different carriers and different functional states of the same carrier will be important for understanding the mechanism and selectivity of substrate transport[29]. Use of RDCs is well suited to this purpose—for example for describing concerted rearrangements of helices, coupled to opening or closing of the carrier on either side of the membrane—as RDCs are sensitive to the relative orientation of structural segments. We emphasize that new methods of measuring side-chain constraints must be developed to provide higher-resolution NMR structures of these carriers and of membrane proteins of comparable size.

METHODS SUMMARY

Mouse UCP2 (residues 14–309, with a C-terminal His$_6$ tag) was expressed using a pET-21 vector in *Escherichia coli* Rosetta DE3 cells. After cell lysis, the lipid

composition of the membrane fraction was adjusted by adding DMPC, cardiolipin and phytanoyl lipids. The protein was extracted using 0.2% DPC in the presence of GDP. The solubilized UCP2 was then subjected to a series of purification steps including Ni-NTA affinity, MonoQ ion exchange, nucleotide-analogue affinity and size exclusion chromatography. The final NMR sample contained 0.8 mM UCP2, 5 mM GDP, 150 mM DPC, 2 mM DMPC, 1 mM cardiolipin, 5 mM β-mercaptoethanol, 30 mM potassium phosphate (pH 6.5), and 80 mM NaCl.

NMR experiments were conducted at 33 °C on spectrometers equipped with cryogenic probes. Sequence-specific assignment of backbone chemical shifts was accomplished using three pairs of triple-resonance experiments and double ^{15}N-edited nuclear Overhauser enhancement spectroscopy, recorded on protein labelled with ^{15}N, ^{13}C and ^{2}H. RDCs were obtained using an aligned sample containing 0.5 mM UCP2 and 20 mg ml^{-1} DNA nanotubes[19] (other components were the same as above). $^1D_{NH}$ was measured by *J*-scaled TROSY-HNCO. $^1D_{C'C\alpha}$ and $^1D_{NC'}$ were measured by TROSY-HNCO with quantitative modulations of $J_{C'C\alpha}$ (the coupling between backbone C' and C$_\alpha$ spins) and $J_{NC'}$ (the coupling between backbone N and C' spins), respectively. To obtain PREs, we generated a Cys-less UCP2 mutant and introduced single cysteines at desired positions for labelling with MTSL (Methods). Residue-specific broadening of protein resonances was measured with two TROSY-HNCO spectra, one recorded after nitroxide labelling and another after reducing the nitroxide free electron with ascorbic acid.

Structure determination had two stages: determination of local structural segments using an RDC-based MFR protocol and determination of the spatial arrangement of the MFR-derived segments using PRE distance restraints. Structures were calculated using XPLOR-NIH[30] with backbone ϕ and ψ values of the assigned structured segments, RDCs and PRE-derived distances. A total of 30 structures were calculated using a simulated annealing protocol, and 15 low-energy structures were selected as the structural ensemble (statistics in Supplementary Table 1).

Full Methods and any associated references are available in the online version of the paper at www.nature.com/nature.

1. Palmieri, F. *et al.* Identification of mitochondrial carriers in *Saccharomyces cerevisiae* by transport assay of reconstituted recombinant proteins. *Biochim. Biophys. Acta* **1757,** 1249–1262 (2006).
2. Krauss, S., Zhang, C. Y. & Lowell, B. B. The mitochondrial uncoupling-protein homologues. *Nature Rev. Mol. Cell Biol.* **6,** 248–261 (2005).
3. Tate, C. G. & Stevens, R. C. Growth and excitement in membrane protein structural biology. *Curr. Opin. Struct. Biol.* **20,** 399–400 (2010).
4. Pebay-Peyroula, E. *et al.* Structure of mitochondrial ADP/ATP carrier in complex with carboxyatractyloside. *Nature* **426,** 39–44 (2003).
5. Mitchell, P. Coupling of phosphorylation to electron and hydrogen transfer by a chemi-osmotic type of mechanism. *Nature* **191,** 144–148 (1961).
6. Aquila, H., Link, T. A. & Klingenberg, M. The uncoupling protein from brown fat mitochondria is related to the mitochondrial ADP/ATP carrier. Analysis of sequence homologies and of folding of the protein in the membrane. *EMBO J.* **4,** 2369–2376 (1985).
7. Zhang, C. Y. *et al.* Uncoupling protein-2 negatively regulates insulin secretion and is a major link between obesity, beta cell dysfunction, and type 2 diabetes. *Cell* **105,** 745–755 (2001).
8. Diao, J. *et al.* UCP2 is highly expressed in pancreatic alpha-cells and influences secretion and survival. *Proc. Natl Acad. Sci. USA* **105,** 12057–12062 (2008).
9. Andrews, Z. B. *et al.* UCP2 mediates ghrelin's action on NPY/AgRP neurons by lowering free radicals. *Nature* **454,** 846–851 (2008).
10. Harper, M. E. *et al.* Characterization of a novel metabolic strategy used by drug-resistant tumor cells. *FASEB J.* **16,** 1550–1557 (2002).
11. Samudio, I., Fiegl, M. & Andreeff, M. Mitochondrial uncoupling and the Warburg effect: molecular basis for the reprogramming of cancer cell metabolism. *Cancer Res.* **69,** 2163–2166 (2009).
12. Schnell, J. R. & Chou, J. J. Structure and mechanism of the M2 proton channel of influenza A virus. *Nature* **451,** 591–595 (2008).
13. Hiller, S. *et al.* Solution structure of the integral human membrane protein VDAC-1 in detergent micelles. *Science* **321,** 1206–1210 (2008).
14. Wang, J., Pielak, R. M., McClintock, M. A. & Chou, J. J. Solution structure and functional analysis of the influenza B proton channel. *Nature Struct. Mol. Biol.* **16,** 1267–1271 (2009).
15. Zhou, Y. *et al.* NMR solution structure of the integral membrane enzyme DsbB: functional insights into DsbB-catalyzed disulfide bond formation. *Mol. Cell* **31,** 896–908 (2008).
16. Van Horn, W. D. *et al.* Solution nuclear magnetic resonance structure of membrane-integral diacylglycerol kinase. *Science* **324,** 1726–1729 (2009).
17. Gautier, A., Mott, H. R., Bostock, M. J., Kirkpatrick, J. P. & Nietlispach, D. Structure determination of the seven-helix transmembrane receptor sensory rhodopsin II by solution NMR spectroscopy. *Nature Struct. Mol. Biol.* **17,** 768–774 (2010).
18. Tjandra, N. & Bax, A. Direct measurement of distances and angles in biomolecules by NMR in a dilute liquid crystalline medium. *Science* **278,** 1111–1114 (1997).

19. Douglas, S. M., Chou, J. J. & Shih, W. M. DNA-nanotube-induced alignment of membrane proteins for NMR structure determination. *Proc. Natl Acad. Sci. USA* **104,** 6644–6648 (2007).
20. Jones, T. A. & Thirup, S. Using known substructures in protein model building and crystallography. *EMBO J.* **5,** 819–822 (1986).
21. Delaglio, F., Kontaxis, G. & Bax, A. Protein structure determination using molecular fragment replacement and NMR dipolar couplings. *J. Am. Chem. Soc.* **122,** 2142–2143 (2000).
22. Shen, Y. *et al.* Consistent blind protein structure generation from NMR chemical shift data. *Proc. Natl Acad. Sci. USA* **105,** 4685–4690 (2008).
23. Raman, S. *et al.* NMR structure determination for larger proteins using backbone-only data. *Science* **327,** 1014–1018 (2010).
24. Losonczi, J. A., Andrec, M., Fischer, M. W. F. & Prestegard, J. H. Order matrix analysis of residual dipolar couplings using singular value decomposition. *J. Magn. Reson.* **138,** 334–342 (1999).
25. Cornilescu, G., Marquardt, J. L., Ottiger, M. & Bax, A. Validation of protein structure from anisotropic carbonyl chemical shifts in a dilute liquid crystalline phase. *J. Am. Chem. Soc.* **120,** 6836–6837 (1998).
26. Battiste, J. L. & Wagner, G. Utilization of site-directed spin labeling and high-resolution heteronuclear nuclear magnetic resonance for global fold determination of large proteins with limited nuclear Overhauser effect data. *Biochemistry* **39,** 5355–5365 (2000).
27. Wang, Y. & Tajkhorshid, E. Electrostatic funneling of substrate in mitochondrial inner membrane carriers. *Proc. Natl Acad. Sci. USA* **105,** 9598–9603 (2008).
28. Dehez, F., Pebay-Peyroula, E. & Chipot, C. Binding of ADP in the mitochondrial ADP/ATP carrier is driven by an electrostatic funnel. *J. Am. Chem. Soc.* **130,** 12725–12733 (2008).
29. Kunji, E. R. & Robinson, A. J. Coupling of proton and substrate translocation in the transport cycle of mitochondrial carriers. *Curr. Opin. Struct. Biol.* **20,** 440–447 (2010).
30. Schwieters, C. D., Kuszewski, J., Tjandra, N. & Clore, G. M. The Xplor-NIH NMR molecular structure determination package. *J. Magn. Reson.* **160,** 66–74 (2002).

Author Contributions M.J.B., W.M.S., S.C.H. and J.J.C. designed the study; M.J.B. prepared NMR samples; M.J.B. and W.M.S. prepared DNA nanotubes; M.J.B. and J.J.C. designed experiments, collected and analysed NMR data, and determined the structure; M.J.B. and J.J.C. wrote the paper; and all authors contributed to editing the manuscript.

Author Information The structure of UCP2 has been deposited in the Protein Data Bank under accession number 2LCK. Reprints and permissions information is available at www.nature.com/reprints. The authors declare no competing financial interests. Readers are welcome to comment on the online version of this article at www.nature.com/nature. Correspondence and requests for materials should be addressed to J.J.C. (chou@cmcd.hms.harvard.edu).

METHODS

Sample preparation. Mouse UCP2 (residues 14–309 with a C-terminal His$_6$ tag) was expressed using a pET-21 vector in *E. coli* Rosetta DE3 cells. After cell lysis, Triton X-100 was added to the lysate at 10 µl per gram of cell pellet, followed by stirring at 4 °C for 2 h in the presence of 10 µM GDP and 0.2% BME. The suspension was homogenized and centrifuged at 1,500g to remove insoluble debris. To adjust the lipid composition of the membrane fraction, 10 mg DMPC, 2 mg cardiolipin and 0.1 mg phytanoyl lipid per gram of cell pellet were solubilized at 20 mg ml^{-1} in 10% octyl glucoside and then added to the supernatant, followed by 2 h of stirring at 4 °C. The membranes were collected by centrifugation at 50,000g for 2 h, and UCP2 was extracted in 40 mM potassium phosphate (pH 8.0), 250 mM NaCl, 50 mM BME, 10 µM GDP and 0.2% DPC. The solubilized UCP2 was adsorbed on a Ni-NTA resin in the absence of GDP and eluted with 300 mM imidazole. The sample was then exchanged by dialysis into low-salt buffer and applied to a MonoQ column. The MonoQ flowthrough was incubated with Ciba Blue nucleotide-analogue resin (Sigma) for 1 h, eluted with 100 µM GDP and, finally, loaded onto a Sephadex S-200 column for size exclusion purification in 50 mM potassium phosphate (pH 6.5), 100 mM NaCl and 5 mM DPC. The eluted UCP2 sample was supplemented with GDP, detergent and lipids such that the final NMR sample contained 0.8 mM UCP2, 5 mM GDP, 150 mM DPC, 2 mM DMPC, 1 mM cardiolipin, 5 mM BME, 30 mM potassium phosphate (pH 6.5) and 80 mM NaCl.

We have also tested expression and purification of mouse UCP1 and UCP3. UCP1 could be expressed and purified as described for UCP2, and showed FFA-dependent proton translocation activity and GDP inhibition. UCP3 could be expressed but presented serious solubility problems during purification.

GDP binding. We used FRET to test GDP binding to UCP2 under the NMR conditions. The intrinsic tryptophan florescence ($\lambda_{ex} = 280$ nm, $\lambda_{em} = 350$ nm) of UCP2 was the resonance energy transfer donor and MANT-GDP ($\lambda_{ex} = 356$ nm, $\lambda_{em} = 440$ nm) was the acceptor. We recorded the emission intensity at 440 nm ($\lambda_{ex} = 280$ nm) of 10 µM UCP2/MANT-GDP complex for increasing GDP concentrations. Figure 1c shows the FRET response as a percentage relative to 1:0 MANT-GDP:GDP. Data were fitted to the standard equilibrium binding equation.

NMR spectroscopy. NMR experiments were conducted at 33 °C on spectrometers equipped with cryogenic TXI probes (Bruker). Sequence-specific assignment of backbone $^1H^N$, ^{15}N, $^{13}C^\alpha$, $^{13}C^\beta$, and $^{13}C'$ chemical shifts were accomplished using three pairs of triple-resonance experiments and a double ^{15}N-edited NOESY, recorded on a protein sample labelled with ^{15}N, ^{13}C and ^2H. The triple-resonance experiments include the TROSY versions of HNCA, HN(CO)CA, HNCACB, HN(CO)CACB, HN(CA)CO and HNCO[31,32]. The ^{15}N-edited NOESY is a high-resolution, 3D (H^N, H^N)-HMQC-NOESY-TROSY with ^{15}N, ^{15}N and $^1H^N$ evolution in the t_1, t_2 and t_3 dimensions, respectively.

The RDCs were obtained by subtracting J of the isotropic sample above from $J + D$ of the aligned sample containing 0.5 mM protein and 20 mg ml^{-1} DNA nanotubes (all other components were the same as in the isotropic sample). Details of preparing DNA nanotubes and aligned protein samples are in Supplementary Information. The sign of the RDC follows the convention that $|^1J_{NH} + ^1D_{NH}| < 92$ Hz when $^1D_{NH}$ is positive. The ^1H–^{15}N couplings were measured at 600 MHz (^1H frequency) using the J-scaled TROSY-HNCO experiment to exploit the favourable relaxation property of the TROSY transitions[33]. In this experiment, two interleaved spectra were recorded, the regular TROSY-HNCO spectrum and a modified TROSY-HNCO spectrum with J_{NH} evolution during the ^{15}N chemical shift evolution scaled to zero. The $^{13}C'$–$^{13}C^\alpha$ couplings were measured at 600 MHz using the 3D TROSY-HNCO experiment with quantitative $J_{C'C\alpha}$ modulations of 0 and 28 ms (ref. 34). The $^{13}C'$–^{15}N couplings were measured at 750 MHz using the 3D TROSY-HNCO experiment with quantitative $J_{NC'}$ modulations of 33 and 66 ms (ref. 35).

To introduce a single paramagnetic site for PRE measurement, the five cysteines of UCP2 were all mutated to alanine or serine (Cys 25 Ala, Cys 191 Ser, Cys 217 Ser, Cys 227 Ser, Cys 256 Ser); the cysteine-free UCP2 had GDP binding properties similar to those of wild-type protein. A single cysteine was introduced into the protein on the basis of the known secondary structures from MFR segments. The

nitroxide baring compound, *S*-(2,2,5,5-tetramethyl-2,5-dihydro-1H-pyrrol-3-yl)methyl methanesulfonothioate (MTSL), was then attached at the cysteine position by adding sevenfold excess label to 10 µM UCP2 in the NMR buffer at pH 8.0, and incubating at 25 °C for 4 h. Excess label was removed to avoid nonspecific broadening. The pH was changed back to 6.5 for NMR measurements. To quantify residue-specific broadening of backbone $^1H^N$, two TROSY-HNCO spectra were recorded, one after nitroxide labelling and the other after reduction of the nitroxide free electron with a ×5 molar ascorbic acid. The same protocol was used to measure broadening of UCP2 resonances by the spin-labelled GDP (Fig. 3c; custom synthesized by Shanghai ChemPartner).

Structure determination. The procedure had two stages: determination of local structural segments by RDC-based MFR and determination of the spatial arrangement of the MFR-derived segments in the tertiary fold using PRE distance restraints. In stage one, we fitted RDCs of every seven-residue stretch along the UCP2 sequence to the fragments in the database using the program PALES[36]. Only those seven-residue stretches with on average more than two RDCs per residue were used for fragment searching. In the end, 5,520 fragments with $Q_{free} < 0.25$ were collected. For each candidate fragment (residue $n - m$) evaluated in the fragment assignment, gap filling or end extension operation (described in the main text), only the ϕ and ψ angles of residue $(n + 1) - (m - 1)$ were used, because the end residues do not have the ^{15}N–$^{13}C'$ dipolar coupling. During fragment assignment, we found that for each seven-residue stretch, the best 5–10 fragments typically have very similar Q_{free} values (differences less than 10%). Therefore, the best fragment was assigned to the region only if these fragments have a backbone root mean squared deviation of less than <0.5 Å. Similarly, there are multiple fragments that score equally well in gap filling or end extension. In those cases, we assigned the best-scoring fragment only if the final merged or extended segments have backbone root mean squared deviation of less than <1 Å. Examples of fragment convergence are shown in Supplementary Fig. 9.

In stage two, we calculated structures using XPLOR-NIH[37] with the assigned structured segments, RDCs and PREs. The ϕ and ψ values of the segments in Fig. 2c are strongly enforced by a harmonic potential with force constant ramped from 10 to 1,000 kcal mol^{-1} rad^{-2}. All RDCs used for determining the segments were applied, and the RDC force constant was ramped from 0.01 to 1.5 kcal mol^{-1} Hz^{-2}. PRE restraints (uncertainties in Supplementary Table 2) were enforced with flat-well harmonic potentials, with the force constant ramped from 1 to 40 kcal mol^{-1} Å^{-2}. In addition to experimental restraints, a weak database-derived 'Rama' potential function[38] was ramped from 0.02 to 0.2 (dimensionless force constant) for the general treatment of side-chain rotamers. A total of 30 monomer structures were calculated using a simulated annealing protocol in which the bath temperature was cooled from 2,000 to 200 K. Fifteen low-energy structures were selected as the structural ensemble (Supplementary Table 1).

31. Salzmann, M., Wider, G., Pervushin, K. & Wuthrich, K. Improved sensitivity and coherence selection for [N-15,H-1]-TROSY elements in triple resonance experiments. *J. Biomol. NMR* **15,** 181–184 (1999).
32. Kay, L. E., Torchia, D. A. & Bax, A. Backbone dynamics of proteins as studied by 15N inverse detected heteronuclear NMR spectroscopy: application to staphylococcal nuclease. *Biochemistry* **28,** 8972–8979 (1989).
33. Kontaxis, G., Clore, G. & Bax, A. Evaluation of cross-correlation effects and measurement of one-bond couplings in proteins with short transverse relaxation times. *J. Magn. Reson.* **143,** 184–196 (2000).
34. Jaroniec, C. P., Ulmer, T. S. & Bax, A. Quantitative J correlation methods for the accurate measurement of $^{13}C'$-$^{13}C^\alpha$ dipolar couplings in proteins. *J. Biomol. NMR* **30,** 181–194 (2004).
35. Chou, J. J., Delaglio, F. & Bax, A. Measurement of one-bond ^{15}N-$^{13}C'$ dipolar couplings in medium sized proteins. *J. Biomol. NMR* **18,** 101–105 (2000).
36. Zweckstetter, M. & Bax, A. Prediction of sterically induced alignment in a dilute liquid crystalline phase: aid to protein structure determination by NMR. *J. Am. Chem. Soc.* **122,** 3791–3792 (2000).
37. Schwieters, C. D., Kuszewski, J., Tjandra, N. & Clore, G. M. The Xplor-NIH NMR molecular structure determination package. *J. Magn. Reson.* **160,** 66–74 (2002).
38. Kuszewski, J., Gronenborn, A. M. & Clore, G. M. Improvements and extensions in the conformational database potential for the refinement of NMR and X-ray structures of proteins and nucleic acids. *J. Magn. Reson.* **125,** 171–177 (1997).